



Modulating metal-oxygen interactions of high-entropy oxide electrocatalysts enables highly-active and ultra-stable water oxidation

Jingyu Wang ^a, Jiahao Zhang ^a, Liyue Zhang ^a, Ling Chen ^{a,*}, Guanjie He ^{b,*}, Hao Jiang ^{a,*}

^a Key Laboratory for Ultrafine Materials of Ministry of Education, Shanghai Engineering Research Center of Hierarchical Nanomaterials, School of Materials Science and Engineering, East China University of Science and Technology, Shanghai 200237, China

^b Electrochemical Innovation Lab, Department of Chemical Engineering, University College London, London WC1E 7JE, UK



ARTICLE INFO

Keywords:
Electrocatalysts
High-entropy oxides
Overpotential
Oxygen evolution reaction

ABSTRACT

High-entropy oxide (HEO) electrocatalysts are appealing for multi-step catalytic reactions as their high compositional diversity and multi-element synergy effects. Herein, we find that the metal-oxygen (M-O) interactions in FeCoNi-based HEO can be well-optimized by introducing Al and Ce elements. The *in-situ* electrochemistry-triggered Al leaching exposes abundant newly-formed active sites with greatly reduced energy difference between TM 3d and O 2p orbitals. This fact shows the enhancement of M-O covalency, which is further quantified by the Fe/Co/Ni charge calculations. The stronger M-O covalency greatly decreases the activation energy of water oxidation at Fe/Co/Ni sites and the barrier of electrical transfer. Furthermore, the Ce element downshifts the O 2p band center, effectively refraining lattice oxygen loss. These advantages enable a supersmall overpotential of 303.7 mV at 500 mA cm⁻² that maintains 95.8 % even operating for 840 h, which is the best report for the HEOs to date.

1. Introduction

Oxygen evolution reaction (OER) is the core half-reaction of the low-carbon electrolytic hydrogen production, rechargeable metal-air batteries and so forth [1–3]. The sluggish reaction kinetics and harsh oxidation environment have brought great challenges to the exploitation of advanced OER electrocatalysts [4–6]. In recent years, high-entropy oxides (HEOs) have attracted great interests because of their high compositional diversity and multi-element synergy effects, which are a class of ideal electrocatalysts for meeting the demands of low-budget, high-activity and long-life [7–9]. Their multiple adsorption sites, which have differentiated adsorption properties, enable the preferential adsorption of various OER intermediates (*OH, *O and *OOH). Besides, the reaction pathway of rate-determined step could be optimized by the efficient transfer and integration of adjacent intermediates, allowing to circumvent the scaling relationship [10–12]. Substantial machine learning and experimental results have proved that FeCoNi ternary oxides (M3Os) are located near the peak position of OER activity volcano plot, the most suitable candidate to replace precious metal based electrocatalysts [13–15]. Notably, their oxygen-related adsorption energy is directly determined by the covalency and ionicity interactions of metal-oxygen (M-O) bonds, giving a benchmark for enhancing the

catalytic ability beyond the volcano summit [16,17].

The optimization of M-O interactions is indispensable for improving catalytic activity and enhancing reaction kinetics [18,19]. Generally, the M-O bonds in FeCoNi-based oxides show a highly-ionic nature due to the Coulomb repulsion enabling d-electron localization, which kinetically impedes the charge transfer [20–22]. Strengthening M-O covalency can expedite the d-electron hopping towards antibonding orbitals, giving rise to the high-spin Fe/Co/Ni species with optimized adsorption properties for reducing reaction barrier [23–25]. For instance, Zhou et al. [26] reported that the accelerated OER kinetics (31.4 mV dec⁻¹) was achieved in ZnFe_xCo_{2-x}O₄ electrocatalysts by Fe-induced greater covalency, which narrows the energy gap between Co 3d and O 2p orbits from 0.81 to 0.75 eV. Grimaud et al. [27] proposed the M-O covalency as a key descriptor for evaluating OER activity of the La_{0.5}Sr_{0.5}CoO₃ electrocatalysts, but the over-elevated covalency led to the movement and transformation of lattice oxygen during OER process, sacrificing the electrochemical stability. Nevertheless, it is a big challenge to accurately modulate their covalency and ionicity for achieving highly-active and ultra-stable HEO electrocatalysts, and the competition mechanism still faces the limited understanding.

Herein, we have reported the M3O-based quinary HEO electrocatalysts with well-balanced M-O interactions by integrating Al and Ce

* Corresponding authors

E-mail addresses: chenling@ecust.edu.cn (L. Chen), g.he@ucl.ac.uk (G. He), jianghao@ecust.edu.cn (H. Jiang).

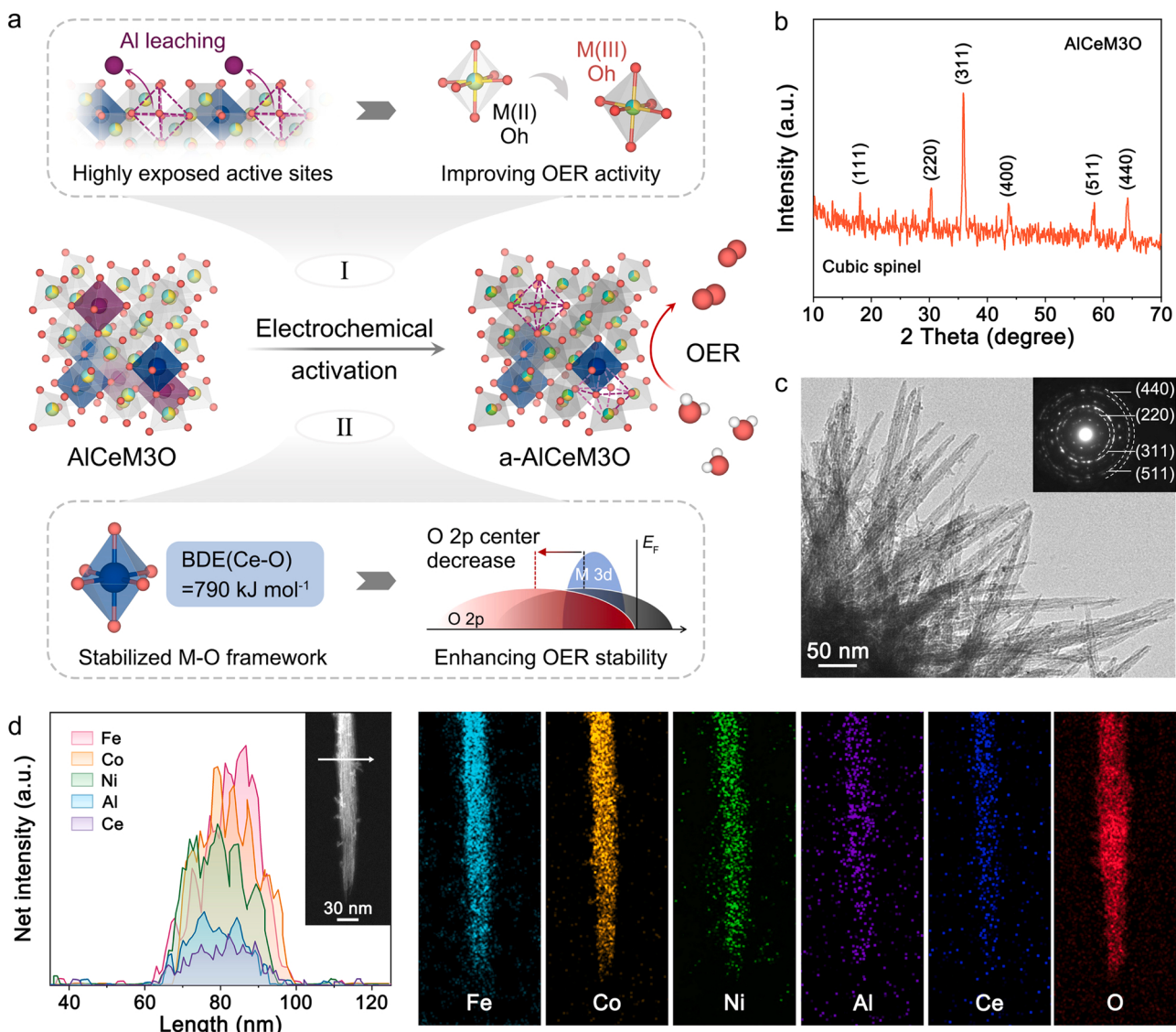


Fig. 1. (a) Design concept and advantages of incorporating Al and Ce in FeCoNi-based HEO electrocatalyst. (b) XRD pattern, (c) high-magnification TEM image (inset showing the corresponding SAED pattern), (d) TEM-EDS line and mapping analyses of AlCeM3O.

elements, in which the *in-situ* Al leaching exposes abundant highly-accessible active sites and enhances the M-O covalency, meanwhile, the Ce element effectively refrains the loss of lattice oxygen by down-shifting the O 2p band center. A supersmall overpotential of 303.7 mV is required to obtain 500 mA cm^{-2} that maintains 95.8 % even operating for 840 h, showing the best report for the HEO electrocatalysts to date.

2. Experimental section

2.1. Material synthesis

For synthesizing the AlCeM3O electrocatalysts, $\text{Fe}(\text{NO}_3)_3 \cdot 9\text{H}_2\text{O}$, $\text{Co}(\text{NO}_3)_2 \cdot 6\text{H}_2\text{O}$, $\text{Ni}(\text{NO}_3)_2 \cdot 6\text{H}_2\text{O}$, $\text{Al}(\text{NO}_3)_3 \cdot 9\text{H}_2\text{O}$ and $\text{Ce}(\text{NO}_3)_3 \cdot 6\text{H}_2\text{O}$ with the molar ratio of 6: 6: 1: 1 were fully blended in a mixer (THINKY, ARE-310) and transferred to a 5 mL flask. A piece of pre-treated Ni foam (thickness of 0.3 mm) was then immersed in the mixture and reacted in a pre-heated muffle furnace at 200°C for 20 min, followed by the quenching treatment. After washing and drying, the AlCeM3O electrocatalysts were obtained by calcining in Ar atmosphere at 500°C for 2 h. Based on the same melting method, the M3O, AlM3O and CeM3O samples were prepared for comparison using the corresponding metal

nitrates.

2.2. Material characterization

The crystallographic structure was recorded by X-ray diffraction (XRD; Rigaku D/Max 2550) adopting $\text{Cu K}\alpha$ radiation operated at 40 kV. The morphology and microstructure were imaged by field emission scanning electron microscopy (FESEM; Hitachi S-4800) and transmission electron microscopy (TEM; FEI Talos F200X) equipped with an energy dispersive spectroscopy (EDS) instrument. The element content was investigated by inductively coupled plasma mass spectrometry (ICP-MS). The surface chemical states were acquired by X-ray photoelectron spectroscopy (XPS; ESCALAB 250Xi) with $\text{Al K}\alpha$ radiation ($\hbar\nu = 1486.6 \text{ eV}$).

2.3. Electrochemical measurements

The electrochemical measurements were carried out by the CHI760E electrochemical workstation using a standard three-electrode cell in 1.0 M KOH electrolyte saturated with high-purity O_2 (99.99 %). The glassy carbon rod and saturated Ag/AgCl electrode were used as the counter

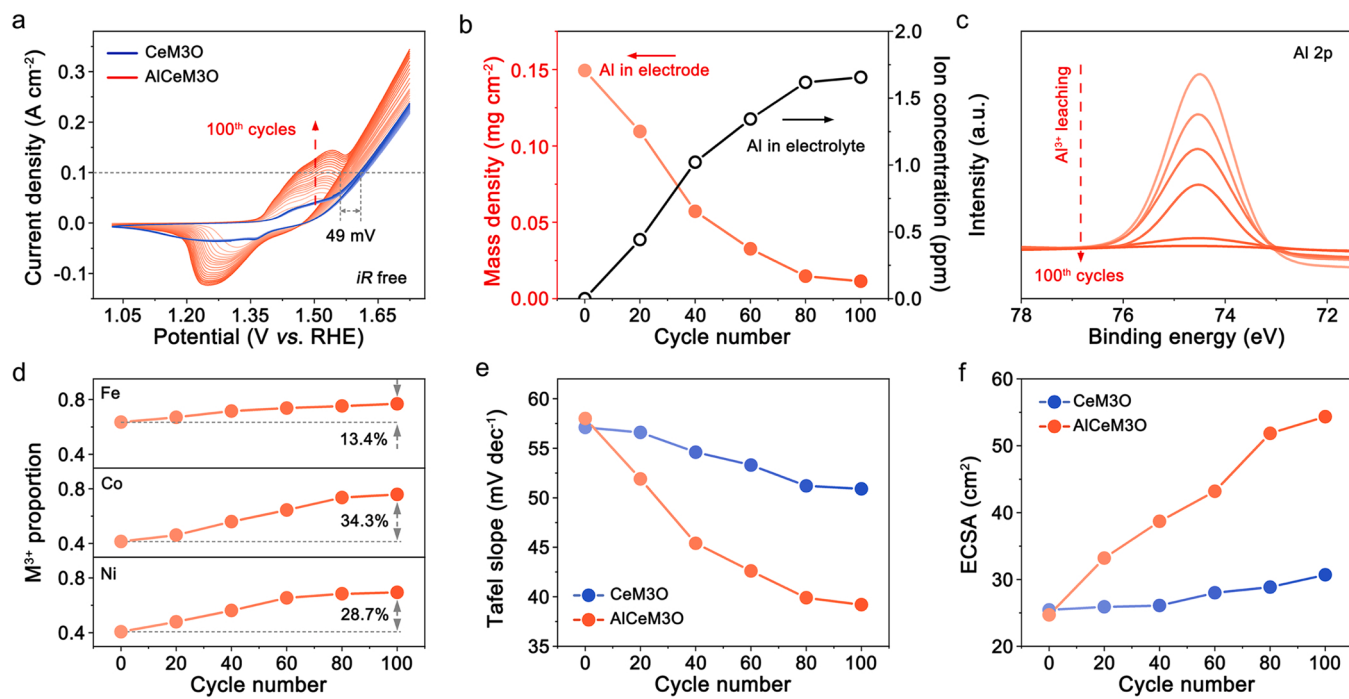


Fig. 2. (a) Electrochemical activation of CeM3O and AlCeM3O in 1.0 M KOH. (b) Dynamic changes of Al content in electrode and electrolyte, (c) Al 2p XPS spectra and (d) M^{3+} proportion of AlCeM3O during CV activation process. (e) Tafel slopes and (f) ECSA values of CeM3O and AlCeM3O at different CV cycles.

and reference electrodes, respectively. The obtained samples were directly used as the working electrodes with a test area of 0.2 cm^2 . Electrochemical activation was performed by cyclic voltammetry (CV) with the scan rate of 50 mV s^{-1} for 100 cycles from 0 to 0.7 V (vs. Ag/AgCl). The samples after electrochemical activation are denoted as a-M3O, a-AlM3O, a-CeM3O and a-AlCeM3O, respectively. The linear sweep voltammetry (LSV) was performed to assess the apparent activity with a scan rate of 2 mV s^{-1} . The Tafel slopes (b) were acquired by fitting the linear portion of the Tafel plots: $\eta = b \log(j) + a$, where η is the overpotential and j is the corresponding current density. The electrochemical surface area (ECSA) was calculated based on the following equation: $\text{ECSA} = C_{\text{dl}} / C_s$, where C_{dl} is the double-layer capacitance and C_s is the specific capacitance. The C_{dl} values were tested via multi-rate CV in non-Faradic range to explore the active site number, while the C_s is $40 \mu\text{F cm}^{-2}$ according to the previous literature [28]. An Autolab PGSTAT302N electrochemical workstation is available for electrochemical impedance spectroscopy (EIS) in the frequency range of 0.01 Hz to 100 kHz. The activation energy (E_a) for oxygen evolution was calculated based on the Arrhenius relationship: $\ln(j) = -E_a / RT + C$, where j is the current density, R is the gas constant ($8.3145 \text{ J mol}^{-1} \text{ K}^{-1}$), and T is the Kelvin temperature. The chronoamperometry (CA) technique was carried out to assess the long-term stability. The electrochemical data are applied with a 95 % iR compensation and calibrated to the reversible hydrogen electrode (RHE) except for special explanation. The calibration of the saturated Ag/AgCl electrode was carried out by the CHI760E electrochemical workstation using a standard three-electrode cell in saturated KCl electrolyte. The reference electrode to be calibrated, bran-new reference electrode and glassy carbon rod were used as the working, reference and counter electrodes, respectively. Calibration is conducted using the $i-t$ measurements under a potential of 0.1 V until the measured open-circuit voltage is within 5 mV.

2.4. Computational details

The density functional theory (DFT) computations were implemented in Vienna *ab initio* simulation package (VASP) with the projector augmented wave (PAW) method and the spin-polarized manner [29].

The Perdew-Burke-Ernzerhof (PBE) functional with the generalized gradient approximation (GGA) was employed for the exchange-correlation functional [30]. The U_{eff} value was set as 4.0 eV for d-orbitals of transition metal in DFT + U method [31]. The medium/high-entropy oxide models were generated based on the Alloy Theoretic Automated Toolkit (ATAT) employed with the special quasi-random structure (SQS) method [32]. In terms of the surface simulations, a vacuum spacing of 10 Å was introduced where the top half layers are relaxed while the bottom half layers are fixed, and the DFT-D3 method was used to correct the Van de Waals interactions between the surface periodic models [33]. The Gamma-center k-point meshes of $3 \times 3 \times 3$ and $2 \times 2 \times 1$ were respectively used for the bulk and surface models with a plane-wave cut-off of 600 eV. The electronic self-consistent field convergence criterion of 10^{-5} eV and a maximum force tolerance for atomic geometry relaxation of $0.03 \text{ eV}/\text{\AA}$ were employed, respectively. The energy difference between intrinsic and defective surfaces, where a certain atom was removed to the vacuum, was calculated to quantify the energy barriers for transition metal dissolution and lattice oxygen loss from electrocatalysts.

3. Results and discussion

To accommodate highly-active and ultra-stable water oxidation, we have designed FeCoNi-based HEO electrocatalysts with Al and Ce incorporation (denoted as AlCeM3O), as illustrated in Fig. 1a. Compared with M3O, Al element has a lower standard electrode potential (Al: -1.66 V versus Fe/Co/Ni: $-0.03/-0.28/-0.25 \text{ V}$), which is inclined to selectively dissolve under alkaline OER conditions [34,35]. Through the electrochemical activation, *in-situ* Al leaching would optimize the electronic state of other metal centers, thereby creating highly accessible active surface for amplifying the synergistic advantage of M3O. On the other hand, Ce element with high M-O bond energy (790 kJ mol^{-1}) could effectively strengthen the M-O framework by band structure modification, making AlCeM3O a robust electrocatalyst with ultra-stable structural chemistry [36,37]. Fig. 1b shows the XRD pattern of the as-prepared AlCeM3O, where the diffraction peaks could be well-indexed to (111), (220), (311), (400), (511) and (440) planes of

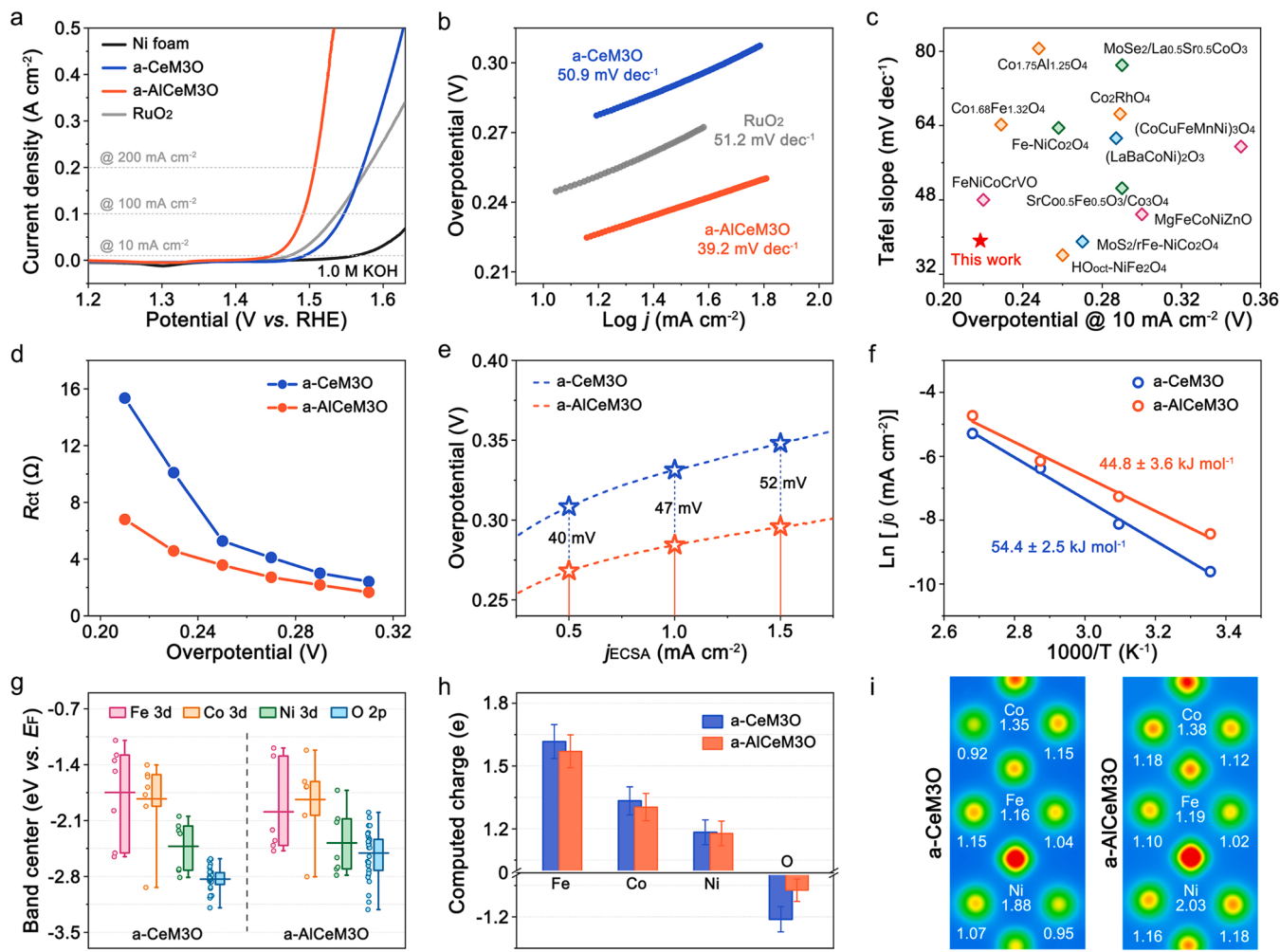


Fig. 3. (a) OER polarization curves and (b) Tafel plots of a-CeM3O and a-AlCeM3O. (c) Performance comparisons among a-AlCeM3O and reported multi-metal oxide catalysts. (d) R_{ct} , (e) j_{ECSA} and (f) E_a of a-CeM3O and a-AlCeM3O. (g) Computed band centers, (h) charge values and (i) 2D charge-density distributions of a-CeM3O and a-AlCeM3O.

cubic spinel structure ($Fd\text{-}3\text{ }m$ space group). No peak splitting demonstrates its single-phase solid solution nature without phase separation [38]. FESEM and TEM images (Figs. S1 & 1c) exhibit that AlCeM3O presents an urchin-like microstructure composed of spines with the width of about 10 nm. Such favorable architecture with abundant connected channels facilitates the electrolyte and bubble diffusion, which is conducive to the electrochemical reaction kinetics [39]. The corresponding selected area electron diffraction (SAED) pattern (insert of Fig. 1c) and high-resolution TEM images (Fig. S2) further verify the well-crystallized spinel structure of AlCeM3O. Additionally, the EDS line-scanning and mapping analyses (Fig. 1d) reveal the homogeneous distribution of Fe, Co, Ni, Al, Ce and O elements in AlCeM3O electrocatalysts.

Electrochemical activation was performed in 1.0 M KOH by CV at 50 mV s⁻¹. As shown in Fig. 2a, AlCeM3O exhibits an equivalent OER activity to CeM3O at the initial stage. Unlike the consistent activity of CeM3O, the oxidation peak and oxygen evolution current of AlCeM3O dramatically raise with cycling, demonstrating the increase in electrochemically accessible sites [40]. After 100 cycles, the CV curve tends to be stable, and the overpotential drops by 49 mV at the current density of 100 mA cm⁻². The M3O and AlM3O represent the similar phenomena (Fig. S3), indicating Al-containing samples display a self-optimization behavior during electrochemical activation process. The real-time Al distribution in electrode and electrolyte was detected by ICP-MS. As exhibited in Fig. 2b, the Al mass density of AlCeM3O gradually decreases

from 0.149 to 0.011 mg cm⁻² along the activation progress and remains at this content level. Accordingly, these leached Al cations are detected in the electrolyte. The dynamic change of XPS signal further witnesses such Al leaching process (Fig. 2c). According to the XPS spectra of other metals (Figs. S4 & 2d), the proportions of trivalent Fe, Co and Ni sites respectively increase by 13.4 %, 34.3 % and 28.7 % as the Al leaching, showing their crucial involvement in OER enhancement. More importantly, raised valency typically induces the downshift of metal d-band to penetrate the p-band of oxygen ligands, resulting in an enhanced M-O covalency along with the Al leaching [23,25]. In contrast, the chemical state of Ce changes insignificantly (Fig. S5). The characterizations after electrochemical activation are exhibited in Fig. S6, showing the *in-situ* formation of highly-active hydroxide species for improving OER properties. Benefiting from their motivated synergistic catalysis, the Tafel slope of AlCeM3O markedly decreases from 58.0 to 39.2 mV dec⁻¹ through electrochemical activation (Figs. S7 & 2e), manifesting its enhanced reaction kinetics with improved OH⁻ adsorption [41]. Furthermore, the AlCeM3O demonstrates the highly exposed active surface as we anticipated, whose ECSA doubles after 100 CV cycles (Figs. S8, S9 & 2f). Based on the above results, we can conclude that the *in-situ* electrochemistry-triggered Al leaching efficiently optimizes the active sites in the AlCeM3O electrocatalysts, thus remarkably improving the OER activity and kinetics.

The alkaline OER performance was assessed in 1.0 M O₂-saturated KOH using the standard three-electrode setup. Figs. 3a & S10 displays

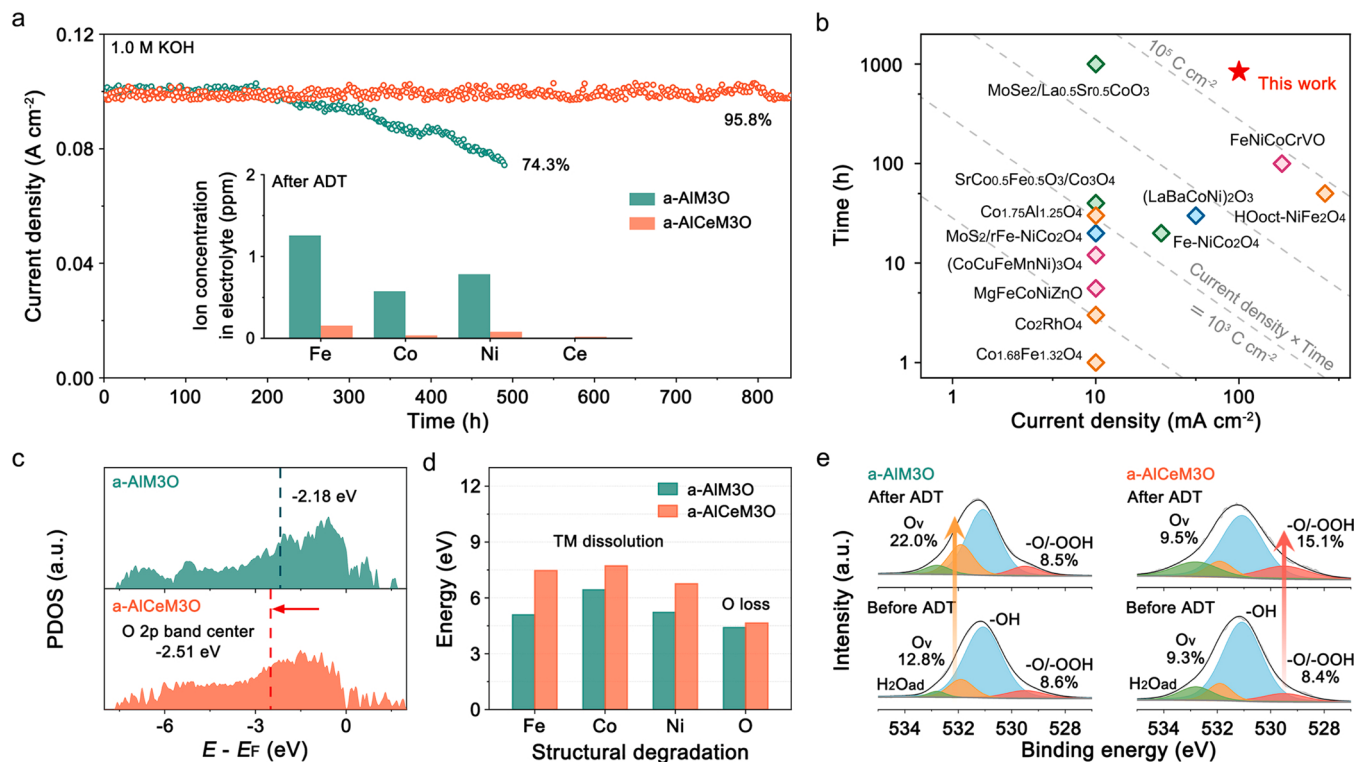


Fig. 4. (a) CA measurements of a-AlM3O and a-AlCeM3O, inset showing the corresponding ion concentrations in electrolyte after ADT. (b) Stability comparison among a-AlCeM3O and reported multi-metal oxide catalysts. (c) Computed O 2p PDOS, (d) energy barriers for transition metal dissolution and lattice oxygen loss of a-AlM3O and a-AlCeM3O. (e) O 1 s XPS spectra of a-AlM3O and a-AlCeM3O before and after ADT.

the polarization curves of the pre-activated samples (denoted as a-CeM3O and a-AlCeM3O), as well as the bare Ni foam and commercial RuO₂. The a-AlCeM3O delivers small overpotentials of 218.5, 261.6 and 303.7 mV at 10, 100 and 500 mA cm⁻², respectively, superior to a-CeM3O ($\eta_{10} = 263.0$ mV; $\eta_{100} = 316.8$ mV) and RuO₂ ($\eta_{10} = 242.9$ mV; $\eta_{100} = 307.0$ mV). It also exhibits the lowest Tafel slope of 39.2 mV dec⁻¹ in comparison with a-CeM3O (50.9 mV dec⁻¹) and RuO₂ (51.2 mV dec⁻¹) (Fig. 3b), suggesting an accelerated reaction kinetics for boosting OER process [42]. Such catalytic properties outperform most reported multi-metal oxide electrocatalysts (Fig. 3c & Table S1). EIS titrations were carried out at a series of overpotentials ranging from 0.21 to 0.31 V (Fig. S11). The a-AlCeM3O is observed to maintain a smaller charge transfer resistance (R_{ct}) throughout the potential range (Fig. 3d), further confirming its rapid electron transfer kinetics [43]. Moreover, the a-AlCeM3O shows a boosted intrinsic activity by comparing the ECSA-normalized current density (j_{ECSA} , Figs. 3e & S12), suggesting that Al leaching could effectively exert synergistic advantage among Fe, Co and Ni sites. Based on the polarization curves at different temperatures (Fig. S13), their corresponding E_a can be calculated. As shown in Fig. 3f, a-AlCeM3O requires only 44.8 ± 3.6 kJ mol⁻¹ for driving alkaline OER, prominently lower than that of a-CeM3O (54.4 ± 2.5 kJ mol⁻¹), indicating the effectively decreased OER energy barrier [44]. DFT calculations were applied to further clarify the OER enhancement mechanism. Fig. 3g summarizes the computed band center statistics of metal and oxygen atoms in each simulation model (Fig. S14). The energy differences between Fe/Co/Ni 3d and O 2p orbitals of a-AlCeM3O are 0.52, 0.67 and 0.13 eV, respectively, much lower than those of a-CeM3O (1.08, 1.00 and 0.41 eV). The smaller energy difference represents stronger M-O covalency, correlating with highly-active water oxidation with expedited charge transfer pathways and optimized adsorption towards oxygen-containing intermediates. More impressively, metal atoms at different locations have differentiated band structure, which is beneficial to enrich the functionality of catalytic sites. As shown in Fig. 3h, the atomic charge values of a-CeM3O and

a-AlCeM3O deviate from the corresponding valence, which is caused by the electron perturbation among M-O bonds and can be quantified as a valid parameter for evaluating their covalency [45]. The a-AlCeM3O displays a higher ionic bias value ($\delta_0 = 0.93$), confirming its enhanced covalent nature. Their representative charge-density distributions from [001] direction are mapped out to visualize the above results. Fig. 3i clearly shows that there are stronger electron interactions in a-AlCeM3O, which is positively correlated with the OER performance.

To examine the long-term OER stability, CA measurements were conducted under the current density of 0.1 A cm⁻². As shown in Fig. 4a, the a-AlCeM3O demonstrates the considerable durability, being able to operate continuously for 840 h (more than a month) with an ultrahigh current retention rate of 95.8 %. In contrast, the apparent activity of a-AlM3O starts to deteriorate rapidly after 240 h until losing efficacy. Moreover, the a-AlCeM3O yields quite less Fe, Co and Ni dissolution (0.15, 0.04 and 0.08 ppm, respectively) in the electrolyte after accelerated durability test (ADT). The structural and compositional changes (Fig. S15 & Table S2) of high entropy oxides are not significantly, confirming its excellent long-term stability. Fig. 4b highlights the stability comparison, in which the gray dashed lines represent the total charge transferred through the electrode, calculated by multiplying the current density by the effective operating time [46]. The a-AlCeM3O exceeds the threshold of 3×10^5 C cm⁻², far surpassing the reported multi-metal oxide catalysts. The stability improvement principle was explored based on DFT calculations. As mentioned above, excessive elevation of O 2p band center (> -2.2 eV vs. E_F) may sacrifice electrochemical stability because lattice oxygen would be activated to participate in OER process [47]. Attributed to the Ce incorporation, the O 2p band center of a-AlCeM3O is successfully modulated from -2.18 to -2.51 eV (Fig. 4c). Consequently, the lattice oxygen framework of a-AlCeM3O is stabilized, whose energy required for oxygen loss (4.65 eV) is remarkably higher than that of a-AlM3O (4.41 eV), as shown in Fig. 4d. Meanwhile, the energy barriers for Fe, Co and Ni dissolution of a-AlCeM3O increase from 5.09, 6.43 and 5.22 eV to 7.47, 7.72 and

6.76 eV, respectively. These results reveal that Ce incorporation plays an important role in improving long-term OER stability by inhibiting surface metal dissolution and lattice oxygen loss, which is consistent with our CA measurements [48]. The corresponding structural degradation processes are illustrated in Fig. S16 & S17. The cross-comparison of O 1 s XPS spectra (Fig. 4e) before and after ADT confirms the theoretical results, showing that the percentage of highly-active species ($^{*}\text{O}/^{*}\text{OOH}$) in a-AlCeM3O increases from 8.4 % to 15.1 %, while the defect degree remains at a moderate level (~ 9.5 %).

4. Conclusion

In summary, we demonstrate that the integration of Al and Ce elements in FeCoNi-based HEO electrocatalysts is responsible for the well-balanced M-O interactions, thus enabling highly-active and ultra-stable water oxidation. Specifically, the *in-situ* Al leaching during electrochemical activation induces the exposure of highly-accessible multi-functional active sites and the enhancement of M-O covalency, leading to highly-oxidized Fe/Co/Ni species for accelerating OER kinetics. Meanwhile, the Ce element significantly stabilizes the M-O framework by inhibiting surface metal dissolution and oxygen loss. Consequently, the a-AlCeM3O exhibits superior OER performance with a small overpotential of 303.7 mV and a low Tafel slope of 33.0 mV dec⁻¹ to realize the current density of 500 mA cm⁻². Furthermore, it demonstrates the considerable stability for continuously operating over 840 h with an ultrahigh current retention rate of 95.8 %, being one of the most advanced multi-metal oxide electrocatalysts to date. This work sheds light on the relationship between M-O interactions and catalytic performance, allowing to improve high-entropy electrocatalysts towards sustainable electrochemical energy technologies.

CRediT authorship contribution statement

Jingyu Wang: Conceptualization, Data curation, Formal analysis, Investigation, Visualization, Writing – original draft. **Jiahao Zhang:** Conceptualization, Formal analysis, Methodology, Writing – original draft. **Liyue Zhang:** Formal analysis. **Ling Chen:** Validation, Project administration, Supervision. **Guangjie He:** Methodology, Writing – review & editing. **Hao Jiang:** Data curation, Funding acquisition, Resources, Supervision, Writing – review & editing.

Declaration of Competing Interest

The authors declare that they have no known competing financial interests or personal relationships that could have appeared to influence the work reported in this paper.

Data availability

Data will be made available on request.

Acknowledgements

This work was supported by the National Natural Science Foundation of China (22208102, U22B20143), and the Fundamental Research Funds for the Central Universities.

Appendix A. Supporting information

Supplementary data associated with this article can be found in the online version at doi:10.1016/j.apcatb.2023.123382.

References

- [1] S. Chu, A. Majumdar, Opportunities and challenges for a sustainable energy future, *Nature* 488 (2012) 294–303.
- [2] J.H. Montoya, L.C. Seitz, P. Chakrhanont, A. Vojvodic, T.F. Jaramillo, J. K. Nørskov, Materials for solar fuels and chemicals, *Nat. Mater.* 16 (2017) 70–81.
- [3] J. Kibsgaard, I. Chorkendorff, Considerations for the scaling-up of water splitting catalysts, *Nat. Energy* 4 (2019) 430–433.
- [4] M.F. Lagadec, A. Grimaud, Water electrolyzers with closed and open electrochemical systems, *Nat. Mater.* 19 (2020) 1140–1150.
- [5] F.-Y. Chen, Z.-Y. Wu, Z. Adler, H. Wang, Stability challenges of electrocatalytic oxygen evolution reaction: from mechanistic understanding to reactor design, *Joule* 5 (2021) 1704–1731.
- [6] Q. Xu, L. Zhang, J. Zhang, J. Wang, Y. Hu, H. Jiang, C. Li, Anion exchange membrane water electrolyzer: electrode design, lab-scaled testing system and performance evaluation, *Energy Chem* 4 (2022), 100087.
- [7] Y. Yao, Q. Dong, A. Brozena, J. Luo, J. Miao, M. Chi, C. Wang, I.G. Kevrekidis, Z. J. Ren, J. Greeley, G. Wang, A. Anapolsky, L. Hu, High-entropy nanoparticles: synthesis-structure-property relationships and data-driven discovery, *Science* 376 (2022), eabn3103.
- [8] A. Sarkar, Q. Wang, A. Schiele, M.R. Chellali, S.S. Bhattacharya, D. Wang, T. Brezesinski, H. Hahn, L. Velasco, B. Breitung, High-entropy oxides: fundamental aspects and electrochemical properties, *Adv. Mater.* 31 (2019), 1806236.
- [9] C.M. Rost, E. Sachet, T. Borman, A. Moballegh, E.C. Dickey, D. Hou, J.L. Jones, S. Curtarolo, J.-P. Maria, Entropy-stabilized oxides, *Nat. Commun.* 6 (2015) 8485–8492.
- [10] Q. Xu, J. Zhang, H. Zhang, L. Zhang, L. Chen, Y. Hu, H. Jiang, C. Li, Atomic heterointerface engineering overcomes the activity limitation of electrocatalysts and promises highly-efficient alkaline water splitting, *Energy Environ. Sci.* 14 (2021) 5228–5259.
- [11] L. Tang, Y. Yang, H. Guo, Y. Wang, M. Wang, Z. Liu, G. Yang, X. Fu, Y. Luo, C. Jiang, Y. Zhao, Z. Shao, Y. Sun, High configuration entropy activated lattice oxygen for O₂ formation on perovskite electrocatalyst, *Adv. Funct. Mater.* 32 (2022), 2112157.
- [12] Z.-F. Huang, J. Song, S. Dou, X. Li, J. Wang, X. Wang, Strategies to break the scaling relation toward enhanced oxygen electrocatalysis, *Matter* 1 (2019) 1494–1518.
- [13] Z. Rao, P.-Y. Tung, R. Xie, Y. Wei, H. Zhang, A. Ferrari, T. Klaver, F. Körmann, P. T. Sukumar, A.K. da Silva, Y. Chen, Z. Li, D. Ponge, J. Neugebauer, O. Gutfleisch, S. Bauer, D. Raabe, Machine learning-enabled high-entropy alloy discovery, *Science* 378 (2022) 78–85.
- [14] M.J. Craig, G. Coulter, E. Dolan, J. Soriano-Lopez, E. Mates-Torres, W. Schmitt, M. García-Melchor, Universal scaling relations for the rational design of molecular water oxidation catalysts with near-zero overpotential, *Nat. Commun.* 10 (2019) 4993–5002.
- [15] L. Han, S. Dong, E. Wang, Transition-metal (Co, Ni, and Fe)-based electrocatalysts for the water oxidation reaction, *Adv. Mater.* 28 (2016) 9266–9291.
- [16] Y. Sun, H. Liao, J. Wang, B. Chen, S. Sun, S.J.H. Ong, S. Xi, C. Diao, Y. Du, J.-O. Wang, M.B.H. Breese, S. Li, H. Zhang, Z.J. Xu, Covalency competition dominates the water oxidation structure-activity relationship on spinel oxides, *Nat. Catal.* 3 (2020) 554–563.
- [17] J. Song, C. Wei, Z.-F. Huang, C. Liu, L. Zeng, X. Wang, Z.J. Xu, A review on fundamentals for designing oxygen evolution electrocatalysts, *Chem. Soc. Rev.* 49 (2020) 2196–2214.
- [18] J. Suntivich, K.J. May, H.A. Gasteiger, J.B. Goodenough, Y. Shao-Horn, A perovskite oxide optimized for oxygen evolution catalysis from molecular orbital principles, *Science* 334 (2011) 1383–1385.
- [19] W.T. Hong, R.E. Welsch, Y. Shao-Horn, Descriptors of oxygen-evolution activity for oxides: a statistical evaluation, *J. Phys. Chem. C* 120 (2016) 78–86.
- [20] Y. Sun, G. Chen, S. Xi, Z.J. Xu, Catalytically influential features in transition metal oxides, *ACS Catal.* 11 (2021) 13947–13954.
- [21] J. Gracia, Itinerant spins and bond lengths in oxide electrocatalysts for oxygen evolution and reduction reactions, *J. Phys. Chem. C* 123 (2019) 9967–9972.
- [22] H. Liu, J. Zhou, L. Zhang, Z. Hu, C. Kuo, J. Li, Y. Wang, L.H. Tjeng, T.-W. Pi, A. Tanaka, L. Song, J.-Q. Wang, S. Zhang, Insight into the role of metal-oxygen bond and O 2p hole in high voltage cathode LiNi_xMn_{2-x}O₄, *J. Phys. Chem. C* 121 (2017) 16079–16087.
- [23] J. Hwang, R.R. Rao, L. Giordano, Y. Katayama, Y. Yu, Y. Shao-Horn, Perovskites in catalysis and electrocatalysis, *Science* 358 (2017) 751–756.
- [24] Z.-F. Huang, J. Song, Y. Du, S. Xi, S. Dou, J.M.V. Nsanzimana, C. Wang, Z.J. Xu, X. Wang, Chemical and structural origin of lattice oxygen oxidation in Co-Zn oxyhydroxide oxygen evolution electrocatalysts, *Nat. Energy* 4 (2019) 329–338.
- [25] N. Zhang, X. Feng, D. Rao, X. Deng, L. Cai, B. Qiu, R. Long, Y. Xiong, Y. Lu, Y. Chai, Lattice oxygen activation enabled by high-valence metal sites for enhanced water oxidation, *Nat. Commun.* 11 (2020) 4066–4076.
- [26] Y. Zhou, S. Sun, J. Song, S. Xi, B. Chen, Y. Du, A.C. Fisher, F. Cheng, X. Wang, H. Zhang, Z.J. Xu, Enlarged Co-O covalency in octahedral sites leading to highly efficient spinel oxides for oxygen evolution reaction, *Adv. Mater.* 30 (2018), 1802912.
- [27] A. Grimaud, O. Diaz-Morales, B. Han, W.T. Hong, Y.-L. Lee, L. Giordano, K. A. Stoerzinger, M.T.M. Koper, Y. Shao-Horn, Activating lattice oxygen redox reactions in metal oxides to catalyse oxygen evolution, *Nat. Chem.* 9 (2017) 457–465.
- [28] Q. Xu, H. Jiang, H. Zhang, Y. Hu, C. Li, Heterogeneous interface engineered atomic configuration on ultrathin Ni(OH)₂/Ni₃S₂ nanoforests for efficient water splitting, *Appl. Catal. B Environ.* 242 (2019) 60–66.
- [29] G. Kresse, D. Joubert, From ultrasoft pseudopotentials to the projector augmented wave method, *Phys. Rev. B* 59 (1999) 1758–1775.
- [30] J. Perdew, K. Burke, M. Ernzerhof, Generalized gradient approximation made simple, *Phys. Rev. Lett.* 77 (1996) 3865–3868.

- [31] S. Dudarev, G. Botton, S. Savrasov, C. Humphreys, A. Sutton, Electron-energy-loss spectra and the structural stability of nickel oxide: an LSDA+U study, *Phys. Rev. B* 57 (1998) 1505–1509.
- [32] A. van de Walle, P. Tiwary, M. de Jong, D. Olmsted, M. Asta, A. Dick, D. Shin, Y. Wang, L. Chen, Z. Liu, Efficient stochastic generation of special quasirandom structures, *Calphad* 42 (2013) 13–18.
- [33] S. Grimme, J. Antony, S. Ehrlich, S. Krieg, A consistent and accurate ab initio parametrization of density functional dispersion correction (DFT-D) for the 94 elements H-Pu, *J. Chem. Phys.* 132 (2010), 154104.
- [34] M. Han, C. Wang, J. Zhong, J. Han, N. Wang, A. Seifitokaldani, Y. Yu, Y. Liu, X. Sun, A. Vomiero, H. Liang, Promoted self-construction of β -NiOOH in amorphous high entropy electrocatalysts for the oxygen evolution reaction, *Appl. Catal. B Environ.* 301 (2022), 120764.
- [35] J. Xie, X. Zhang, H. Zhang, J. Zhang, S. Li, R. Wang, B. Pan, Y. Xie, Intralayered Ostwald ripening to ultrathin nanomesh catalyst with robust oxygen-evolving performance, *Adv. Mater.* 29 (2017), 1604765.
- [36] H. Xu, J. Cao, C. Shan, B. Wang, P. Xi, W. Liu, Y. Tang, MOF-derived hollow CoS decorated with CeO_x nanoparticles for boosting oxygen evolution reaction electrocatalysis, *Angew. Chem. Int. Ed.* 57 (2018) 8654–8658.
- [37] J. Li, Z. Xia, M. Zhang, S. Zhang, J. Li, Y. Ma, Y. Qu, Ce-doped CoS₂ pyrite with weakened O₂ adsorption suppresses catalyst leaching and stabilizes electrocatalytic H₂ evolution, *J. Mater. Chem. A* 7 (2019) 17775–17781.
- [38] J. Wang, J. Zhang, Y. Hu, H. Jiang, C. Li, Activating multisite high-entropy alloy nanocrystals via enriching M-pyridinic N-C bonds for superior electrocatalytic hydrogen evolution, *Sci. Bull.* 67 (2022) 1890–1897.
- [39] V.H. Hoa, D.T. Tran, H.T. Le, N.H. Kim, J.H. Lee, Hierarchically porous nickel-cobalt phosphide nanoneedle arrays loaded micro-carbon spheres as an advanced electrocatalyst for overall water splitting application, *Appl. Catal. B Environ.* 253 (2019) 235–245.
- [40] J. Ding, T. Fan, K. Shen, Y. Li, Electrochemical synthesis of amorphous metal hydroxide microarrays with rich defects from MOFs for efficient electrocatalytic water oxidation, *Appl. Catal. B Environ.* 292 (2021), 120174.
- [41] J. Zhang, T. Quast, W. He, S. Dieckhöfer, J.R.C. Junqueira, D. Öhl, P. Wilde, D. Jambrec, Y.-T. Chen, W. Schuhmann, In situ carbon corrosion and Cu leaching as a strategy for boosting oxygen evolution reaction in multimetal electrocatalysts, *Adv. Mater.* 34 (2022), 2109108.
- [42] D. Liang, C. Lian, Q. Xu, M. Liu, H. Liu, H. Jiang, C. Li, Interfacial charge polarization in Co₂P₂O₇@N_x co-doped carbon nanocages as Mott-Schottky electrocatalysts for accelerating oxygen evolution reaction, *Appl. Catal. B Environ.* 268 (2022), 118417.
- [43] B. Yang, N. Zhang, G. Chen, K. Liu, J. Yang, A. Pan, M. Liu, X. Liu, R. Ma, T. Qiu, Serpentine Co_xNi_{3-x}Ge₂O₅(OH)₄ nanosheets with tuned electronic energy bands for highly efficient oxygen evolution reaction in alkaline and neutral electrolytes, *Appl. Catal. B Environ.* 260 (2020), 118184.
- [44] X. Qiao, H. Kang, Y. Li, K. Cui, X. Jia, X. Wu, W. Qin, Grain boundary density and electronic dual modulation of intermetallic Co₂B by Fe doping toward efficient catalyst for oxygen evolution reaction, *Appl. Catal. B Environ.* 305 (2022), 121034.
- [45] S. Sun, Y. Sun, Y. Zhou, S. Xi, X. Ren, B. Huang, H. Liao, L.P. Wang, Y. Du, Z.J. Xu, Shifting oxygen charge towards octahedral metal: a way to promote water oxidation on cobalt spinel oxides, *Angew. Chem. Int. Ed.* 58 (2019) 6042–6047.
- [46] A. Li, S. Kong, C. Guo, H. Ooka, K. Adachi, D. Hashizume, Q. Jiang, H. Han, J. Xiao, R. Nakamura, Enhancing the stability of cobalt spinel oxide towards sustainable oxygen evolution in acid, *Nat. Catal.* 5 (2022) 109–118.
- [47] K.J. May, C.E. Carlton, K.A. Stoerzinger, M. Risch, J. Suntivich, Y.-L. Lee, A. Grimaud, Y. Shao-Horn, Influence of oxygen evolution during water oxidation on the surface of perovskite oxide catalysts, *J. Phys. Chem. Lett.* 3 (2012) 3264–3270.
- [48] Z.-Y. Wu, F.-Y. Chen, B. Li, S.-W. Yu, Y.Z. Finfrock, D.M. Meira, Q.-Q. Yan, P. Zhu, M.-X. Chen, T.-W. Song, Z. Yin, H.-W. Liang, S. Zhang, G. Wang, H. Wang, Non-iridium-based electrocatalyst for durable acidic oxygen evolution reaction in proton exchange membrane water electrolysis, *Nat. Mater.* 22 (2023) 100–108.